Review Article

A Review on Analysis Method of Proximal Hyperspectral Imaging for Studying Plant Traits

Jian Wen Lin, Mohd Shahrimie Mohd Asaari*, Haidi Ibrahim, Mohamad Khairi Ishak dan Abdul Sattar Din

School of Electrical and Electronic Engineering, Universiti Sains Malaysia, 14300 USM, Pulau Pinang, Malaysia

ABSTRACT

Understanding the response of plant traits towards different growing conditions is crucial to maximizing crop yield and mitigating the effect of the food crisis. At present, many imaging techniques are being explored and utilized within plant science to solve problems in agriculture. One of the most advanced imaging methods is hyperspectral imaging (HSI), as it carries the spectral and spatial information of a subject. However, in most plant studies that utilized HSI, the focus was given to performing an analysis of spectral information. Even though a satisfactory performance was achieved, there is potential for better performance if spatial information is given more consideration. This review paper (1) discusses the potential of the proximal HSI analysis methods for plant traits studies, (2) presents an overview of the acceptance of hyperspectral imaging technology for plant research, (3) presents the basic workflow of hyperspectral imaging in proximal settings concerning the image acquisition settings, image pre-processing, spectral normalization, and spectral analysis, (4) discusses the analysis methods that utilize spatial information, and (5) addresses some technical challenges related to implementing hyperspectral imaging in proximal settings for plant traits analysis.

INTRODUCTION

Food crisis arises from extreme climates, such as droughts and heat waves, that might cause the crops to yield, unable to meet the supply-demand for human consumption in

the future. The current trends of agriculture yield that increased by 1.6%, 1.0%, 0.9%, and 1.3% each year for maize, rice, wheat, and soybean, respectively, were still insufficient to meet the demand of the projected population by 2050 (Ray et al., 2013). A recent study reported that for each degree-Celsius increase in global mean temperature, crops like wheat, maize, rice, and soybean would decrease at a single-digit percentage rate (Zhao et al., 2017). Therefore, to boost the global crop yield, one of the solutions is to breed more sustainable crops that can survive through extreme biotic and abiotic stresses.

The understanding of the plant's response to different biotic and abiotic stresses is known as plant phenotyping. Plant phenotyping is particularly important to support the decision-making in breeding higher-quality crops (Li et al., 2014). For instance, Sims and Gamon (2002) used measurement of the Xanthophyll-cycle pigment content, which is associated with spectral reflectance in the visible green region (500 nm–570 nm) in plants to estimate photosynthesis efficiency and, thus, could accelerate research of plant resistance towards stress. The discovery of such plant traits towards stress might take years due to the limitation of imaging sensors. Examples of traditional imaging sensors used to obtain plant traits were Red-Green-Blue (RGB), fluorescence, thermal, and multispectral cameras. Comparing these traditional imaging sensors with the promising hyperspectral (HS) camera, the latter captures more information in a single image. As technology advances, HS cameras become more accessible for research imaging purposes, leading to increased studies conducted using HS cameras.

HS camera has been widely used in plant phenotyping due to its capability to capture a wide range of spectral reflectance from samples. Technically, the spectral information acquired by several types of HS cameras ranges from visible light (VIS) to shortwave-infrared (SWIR), which is a wavelength from 400 nm to 2500 nm (Salazar-vazquez & Mendez-vazquez, 2020). As a comparison with the conventional RGB camera, the HS camera provided more information for plant phenotyping as many plant traits and chemical interactions that happened in plants corresponded to electromagnetic waves within the spectrum range of near-infrared (NIR) and SWIR (Nguyen & Lee, 2006; Sims & Gamon, 2003). In most common approaches, many vegetation indices (VI) derived within the NIR-SWIR wavelength region, like normalized difference vegetation index (NDVI), red edge normalized ratio (NR red edge), water index (WI), and moisture stress index (MSI) were used to determine different biophysical conditions of plants (Zhang & Zhou, 2019). Besides, the absorption valley of electromagnetic waves was also used to estimate the water content of corn leaves located between 900 nm and 1700 nm (Sun et al., 2021).

A multispectral camera is another imaging device that works similarly to the HS camera. However, the HS camera was more favored as the HS images carried more detailed information than multispectral images. The spectral signature of HS images can be considered a continuous spectrum as the interval between captured spectral bands was small.

However, this technical feature was less prominent for the multispectral images because the spectral bands were captured far from each other. Therefore, the spectral signature was considered discrete for the multispectral image. The greater spectral dimensionality of HS images allowed a more in-depth examination and discrimination of the plant's responses. The abundant amount of information carried by HS images attracted the attention of researchers and has led to an increase in technical papers discussing hyperspectral imaging (HSI) analysis in the agriculture field compared to past decades (Lu et al., 2020).

Since HSI emerged as a promising method for plant phenotyping, the imaging methods can be categorized into remote sensing and proximal imaging, as Goetz (2009) demonstrated. Remote sensing refers to capturing a large area of objects within a single image. For example, the common Indiana Pines and University of Pavia datasets were obtained from the HSI satellite and, thus, considered remote sensing. Besides, remote sensing includes unmanned aerial vehicles (UAV) and aircraft, which allows a large area of targets to be captured simultaneously. In contrast to remote sensing, proximal imaging denotes the distance of 1 meter between sensors and plants (Mishra, Lohumi et al., 2020). Proximal HSI is usually carried out indoors in a laboratory or greenhouse area. The time taken for proximal HSI is longer for the whole group of samples as the sample image is usually taken one at a time. However, with the development of a high-throughput phenotyping platform (HTPP), the proximal HSI can be performed efficiently and with minimal human intervention.

Mainly, the information carried by HS images can be categorized into two, which are spectral and spatial information (Saha & Manickavasagan, 2021; Zhang & Zhou, 2019). The common downsides of processing HS images are high computational cost and long processing duration. Therefore, numerous studies were carried out to determine the most efficient algorithm for the HS image. However, most studies only utilized the spectral information from HS images for the proximal analysis of plants. It might have wasted a large amount of spatial information, which could play a significant role in studying plant traits.

This paper aims to provide insights into HSI workflow and how spatial information is utilized throughout the proximal HSI analysis.

WORKFLOW OF PROXIMAL HYPERSPECTRAL IMAGING

The spectral and spatial information obtained from HS images can be redundant and frequently accompanied by noises. Therefore, several algorithms were developed for effective information extraction in different use cases, like detecting plant traits when experiencing water stress, disease, or lacking certain nutrients. Even though the set-up of imaging stations and algorithms might differ in these studies, the general technical workflow of proximal HSI analysis of plants was similar. The workflow can be categorized into image acquisition, image pre-processing, and spectral modeling. Illumination correction belongs

to the pre-processing stage. However, as the illumination effect is a major concern in HSI analysis, it will be discussed in more detail later. Figure 1 shows the flowchart of the general workflow of HSI analysis for better illustration.

Image Acquisition

The acquisition of HS images was challenging as multiple factors needed to be considered before setting up the imaging station to ensure that the obtained HS images had less noise and an efficient acquisition process. Types of HS cameras, illumination sources, and acquisition geometry arrangement were among the factors.

In general, the HS cameras used to capture plant images can be performed in three separate ways, such as whiskbroom, pushbroom, and tunable filter, as shown

Figure 1. Flowchart for the general workflow of proximal HSI analysis

in Figure 2, in which each method has its advantages and disadvantages (Elmasry et al., 2012). For the whiskbroom method, firstly, a grid of spatial position was predefined on the sample surface. Then, the camera scanned the spectrum of a single point at a time. The advantage of the whiskbroom method was that the illuminations for every point passed through the optical system similarly. However, the whiskbroom method caused spatial distortion in HS images, and the time taken for a complete scan was much longer than other methods (Stuart et al., 2019). The pushbroom method utilized a two-dimensional dispersing element and detector array to obtain the sample's HS image (line by line). Due to their speed and versatility, the pushbroom HS cameras were commonly installed in conveyor-belt systems like HTPP for effective sample image acquisition (Manley et al., 2009). Lastly, the tunable filter HS camera acquired the samples images by capturing the spectrum of all points according to their wavelength by using liquid crystal tunable filters (LCTF) or acousto-optic tunable filters (AOTF) (Gupta et al., 1999; X. Wang et al., 2018). No movement of either the camera or the sample was allowed throughout the process. The acquisition duration of the tunable filter method depended on the number of spectral bands concerned. Therefore, using the tunable filter method was most practical only when the interested spectral bands were less.
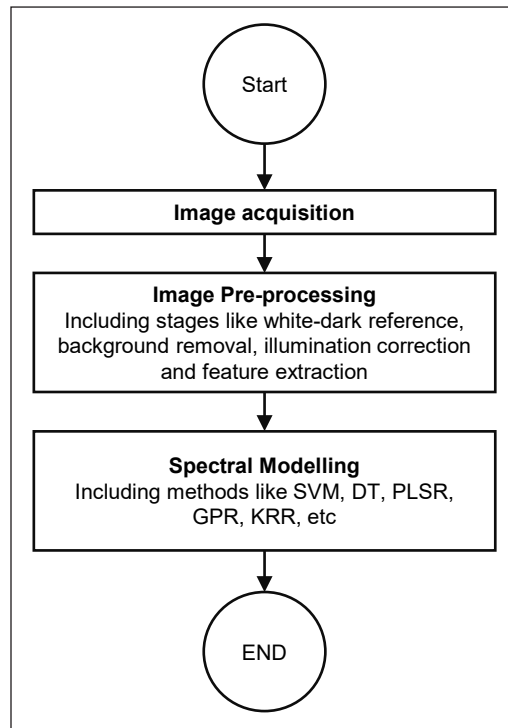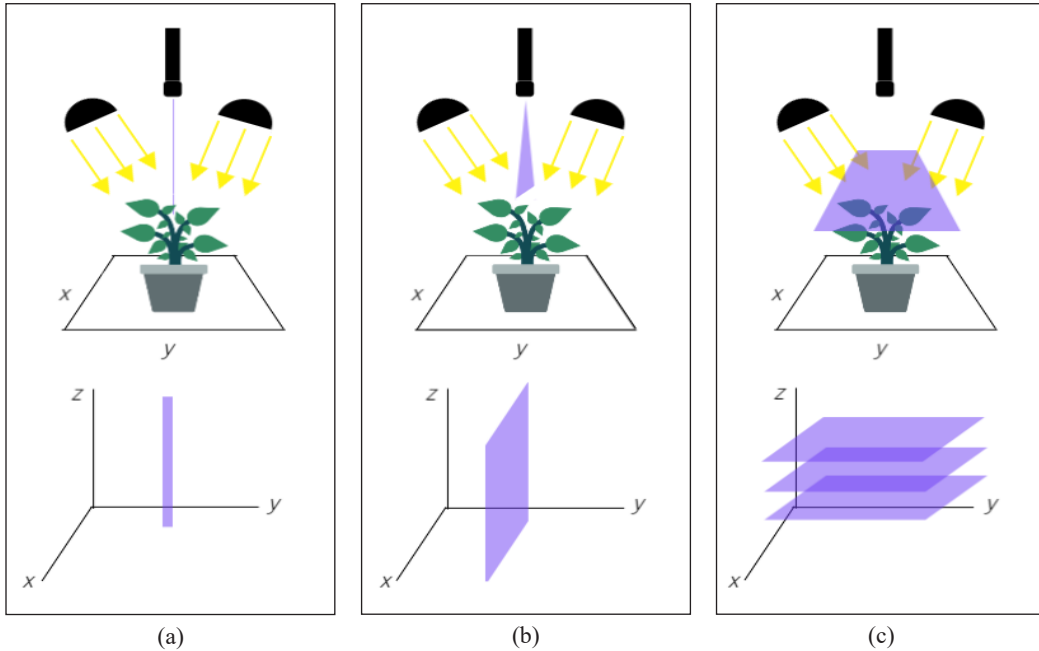
Figure 2. Illustration of: (a) whiskbroom; (b) pushbroom; and (c) tunable imaging method

Another important consideration during image acquisition was the illumination sources. The illumination sources can be categorized into two: passive and active light sources (Grönwall et al., 2016). A passive light source is a natural light, usually used when the image acquisition station is outdoors or in a greenhouse. In some passive light source use cases, special glass was used to filter the sunlight spectrum so that only interested bands were used for analysis. Meanwhile, the active light sources consist of man-made devices, such as tungsten halogen lamps, gas discharge tubes, xenon lamps, and the ubiquitous light-emitting diode (LED) lamps. When choosing an active light source, the set-up convenience, cost, and interest bandwidths need to be considered. Figure 3 shows the set-up of different illustration source directions. In plant phenotyping, halogen lamps were used as their illumination, which ranged from 400 nm–to 2600 nm, which allowed the HS image to be captured (Paulus & Mahlein, 2020). Table 1 lists the image acquisition criteria of studies relevant to proximal HS crop analysis.
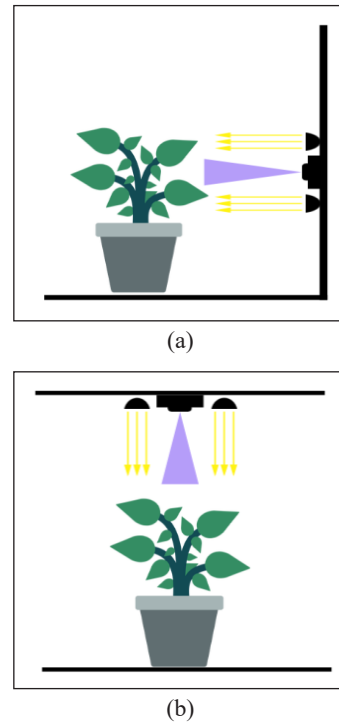

Figure 3. Illustration of image acquisition: (a) Side; and (b) top

Image Pre-processing

The first HS image obtained by the camera was considered raw data that contained noises and pixels that were not parts of the sample. At this stage, these raw signals were heavily affected by spectral non-uniformities and could not be used directly for quantitative analysis. Therefore, pre-processing steps were required to extract clean and useful data for an accurate analysis. The remaining part will discuss the common steps used to obtain useful data from the HS image of a plant.

Once the HS image was captured, a radiometric calibration of the camera needed to be performed to reduce the effect of uneven illumination. The original reflectance value of each band will be converted to a relative reflectance value by using Equation 1.

$$R = \frac{I-B}{W-B} \tag{1}$$

Where R represents the calibrated HS image, I is the raw HS image, B is the image obtained when the HS camera shutter was completely covered (black reference), and W is the HS image of a high-reflective whiteboard (white reference). After this step, the relative reflectance value ranged from 0 to 1, and thus, the effect of outliers due to uneven illumination was reduced.

Depending on the position and the distance of the HS camera with the targeted plants, the captured HS image may contain background objects that were not part of the plants, such as soil, pot, and the imaging platform. It was important to focus only on the plant pixels for further analysis. Image segmentation techniques were applied to suppress the background pixels. In studying plant traits' response to drought, Behmann et al. (2016) applied k-mean clustering to segment HS images into plant and background clusters. Plant clusters were defined using a normalized difference vegetation index (NDVI) with a threshold of 0.3 and a near-infra-red (745 nm) threshold of 0.3 for the cluster centroid. For the NDVI calculation, reflectance values of bands 670 nm and 800 nm, within the red visible and near infra-red (NIR) range, respectively, were used in the calculation using Equation 2.

$$NDVI = \frac{R_{800}-R_{670}}{R_{800}+R_{670}} \tag{2}$$

The values calculated after Equation 2 ranged from -1 to +1. The NDVI value must be at least 0.2 or above, in which a higher value represents denser vegetation to ensure that a pixel belongs to a plant. The NDVI value, near 0, usually indicates objects like rock, sand, or snow, while a negative NDVI value indicates water.

Illumination Correction

Spectral Averaging. Spectral averaging is a straightforward illumination correction method (Pandey et al., 2017). It is implemented by averaging the spectral signature of

all pixels that belong to a plant in an HS image. The average spectrum lost all the spatial information, which could be useful for further analysis. Besides, spectral averaging assumes that noise to the spectra will be minimized by mixing normal and noisy spectra. Despite requiring a low computational cost, spectral averaging is not recommended for reducing noise-like illumination effects. The accuracy of spectral averaging is highly dependent on the segmentation step. If the pixels used for averaging are contaminated by pixels not part of the sample, the resulting spectrum will not be able to represent the plant accurately.

Spectral Smoothing. Spectral smoothing is a spectral correction method that mitigates the effect of spiky noise in the spectrum caused by the illumination effect. The variations of spectral smoothing are like moving average, first derivatives, second derivatives, and Savitsky-Golay (SG) polynomials filter (Fletcher & Turley, 2017). A smoothed spectrum has a higher Signal-to-Noise Ratio (SNR) as the noise carried by spiky bands is shared among the adjacent reflectance values. The computational power of spectral smoothing can be a few times higher depending on the derivative function used. Besides, the number of bands in the smoothed spectrum will be lesser than in the original spectrum.

Standard Normal Variate. The standard normal variate (SNV) normalization improves spectral averaging by retaining the spatial information of HS images. SNV normalization is inspired by chemometrics domains, whereby the formula models light scattering when light is reflected from the sample surface (Asaari et al., 2018; Vigneau et al., 2011). Firstly, the leaf surface was assumed to be a Lambertian surface where the reflectance intensity was similar in all directions. Therefore, the factor that greatly affected the reflectance received by the camera would be the leaf inclination. Coupled Lambert's cosine law with inverse square law (Brownson, 2014). The following Equation 3 describes the SNV normalization computation:

$$Z = \frac{X - X_{mean}}{X_{std}} \qquad\qquad (3)$$

Where X is the original processed reflectance value across all bands for one pixel. X_{mean} and X_{std} are the mean and standard deviation of X for all sample pixels, and Z is the normalized spectra. Note that SNV normalization is performed on the individual spectrum. Thus, no averaging of the spectrum is required.

Multiple Scattering Correction (MSC). The Multiple Scattering Correction (MSC) normalization is very similar to SNV normalization as both normalization methods were inspired by chemometrics. The only difference between SNV and MSC is that MSC normalization requires a reference spectrum. Most studies used the average spectrum as a reference spectrum as it is deemed free from noise. However, as mentioned above,

the average spectrum is very sensitive to outliers, which are non-sample spectra. Such characteristic causes MSC normalization to be more susceptible to noise. Even so, MSC normalization is still a popular correction method and has been applied in many HS studies due to its longer history compared to SNV normalization. For instance, Ren et al. (2020) employed it to correct the HS spectrum of black tea samples.

Variable Sorting Normalization. Variable sorting normalization (VSN) is a recent development for spectral correction by Mishra, Polder et al. (2020) and was used together with illumination correction methods, such as SNV, MSC, and Detrend. For example, when coupled with SNV, VSN estimated the weight for each wavelength in the computation of weight and standard deviation of the HS image. In another work, Fischler and Bolles (1987) performed estimation via a random sample consensus (RANSAC) algorithm, which calculated the dependency of each wavelength towards size effects (addition and multiplication offsets). With VSN, the illumination correction methods can model the illumination scattering with the least influence of chemical variables.

Spectral Processing

Band Selection and Feature Extraction. Dense sampling due to small band intervals caused another redundancy of information. Not all values were useful for HS analysis, and retaining such data would impose a higher computational cost for the analytic process. Therefore, band selection and feature extraction were two important approaches to remove data that was insignificant to the analysis result.

In-band selection, the number of spectral bands was reduced by selecting a subset of the most discriminating features, which minimized the reconstruction error rate. The common techniques for performing band selection are analysis of variance Fisher (ANOVA F-test), random forest (RF), and sequential forward selection (SFS). The intensity values were grouped according to spectral bands in the ANOVA F-test. Each spectral band group consists of several values equivalent to the number of pixels of an image. Then, the same waveband group of images from different treatment groups was compared using ANOVA. Spectral bands with an F1 score lower than the preset threshold were considered a less significant spectral band and were removed. The ANOVA F-test had successfully been used as one of the pre-processing steps in identifying rice of different genotypes. Sabzi et al. (2021) detected excess nitrogen consumption in cucumbers (Wang et al., 2010). RF was used by Dinç and Aygün (2013), whereby a feature in a supervised self-training classifier formed each classification tree. Each classification tree had its voting result and was combined to form the final voting result. The classification result with the largest number of votes determined the final feature category. Even though RF was a promising classifier, it required a large amount of sampling data and features to prevent overfitting. The trained

RF was used on unlabeled inputs to apply RF as band selection. Certain features were selected, and all their values were shuffled for all the unlabeled inputs before the mean squared error (MSE) was computed. A large MSE indicated an important feature. In the case of SFS, classification was first performed separately for each feature. The feature which had the highest predictive accuracy was added to a subset. Several works have shown the feasibility of SFS in reducing the high-dimensional HS data prior to classification (Bradley et al., 2018).

In feature extraction, a new set of features was created by transforming the data into a new feature space. A common feature extraction technique used on HS data was based on a linear combination of image bands, such as in principle component analysis (PCA) and minimum noise fraction (MNF). As mentioned previously, the HS image consists of more than hundreds of bands, and this information can be redundant. Rodarmel and Shan (2002) stated that PCA works on the assumption that all neighboring bands of the HS vector highly correspond to each other. Therefore, PCA aimed to minimize the correlation between bands and obtain an optimum linear band combination that retained most information in the original data. The dataset obtained from PCA was known as principal components and was arranged by the amount of original information retained descending. In most situations, only the first few principal components would be used for further analysis. Figure 4 illustrates the PCA applied in data with 2 bands, also known as dimensions. In Figure 4, each data contained a value of Band 1 and Band 2, which can be represented as in Equation 4.

$$m_i = \left(x_{f1}, x_{f2}\right) \qquad (4)$$

Highly correlated data can be represented in a lesser number of bands. Figure 4 shows PCA Band 1, which retained most of the variations of the original data with just a single band. Any further classification processes applied in PCA Band 1 would obtain a similar result as applied in the original data, which consists of Band 1 and Band 2. A more comprehensive mathematical derivation and historical review of PCA can be referred to in a study by Gonzalez and Woods (1993).

Meanwhile, MNF is a 2-step linear transform denoising technique for HS images. The first step is known as 'noise-whitening,' using principal components of the noise covariance matrix to decorrelate and rescale the noise in data. After the first
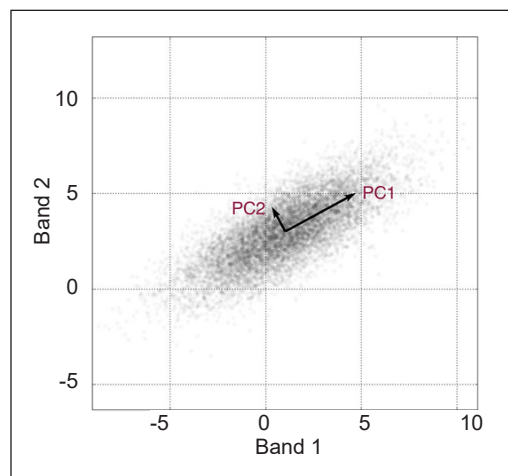

Figure 4. Illustration of PCA

step, the resulting data would have noise with unit variance and minimum correlation between bands. The second step was conducted by applying PCA to the noise-whitened data. A previous study showed that MNF achieved a higher signal-to-noise Ratio (SNR) as compared to PCA for signal-dependent noise (Luo et al., 2016). However, the PCA result had higher SNR than MNF when dealing with Gaussian white noise. The mathematical steps of MNF were explained in detail in a study by Nielsen (2011).

Spectral Modelling. Pre-processing data will be fed into machine learning models for either classification or regression approaches. Table 2 shows the spectral modeling methods, illumination correction, and feature extraction implemented in proximal HSI analysis. The classification approach aims to locate inputs into the correct class, respectively, while the regression approach predicts the output quantity for a given input value. Some of the most common classifiers, such as support vector machine (SVM) and decision tree (DT), whereas models like partial least square regression (PLSR), Gaussian process regression (GPR), and kernel ridge regression (KRR) were considered as regression approaches**.**

Support Vector Machine (SVM). SVM classified data into two groups by forming a hyperplane within the high-dimensional data with the largest support vector margin. The hyperplane could be in different shapes by using SVM with kernel functions, such as polynomial, linear, and radial basis functions. Figure 5 shows an illustration of a linear SVM methodology. Data were classified into circle and triangle groups by a decision hyperplane between two support vectors.

Moughal (2013) used SVM together with minimum noise fraction (MNF) to analyze HS data, and the overall accuracy was the highest among maximum likelihood (ML) and spectral angle mapper (SAM) classifiers. In a recent study, Guo et al. (2019) showed that HS data was first reduced using PCA, and the first three PCs were fed into a guided filter in Equation 5 as a noise reduction and image dehazing step.

$$q_i = \alpha_k g_i + b_k \forall \iota \varepsilon \omega_k \qquad (5)$$

Where q is the linear transform of g in a window ω_k centered at pixel k. α_k and b_k are linear coefficients and bias. After the image was filtered, SVM was adopted to classify the image pixel by pixel.
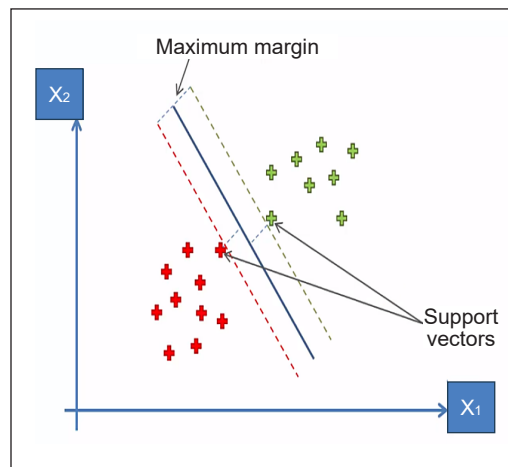

Figure 5. Illustration of SVM

Decision Tree (DT). As a comparison with other classifiers, DT was less computationally intensive and provided good readability. It adopted the top-down recursive strategy in which each leaf node denoted the classified class of a feature. The branch with the least conflict with the training data set decided on the input class. The correct classification rate (CCR) using Equation 6 to predict the performance of a DT model.

$$CCR = \frac{N_c}{N_t} \times 100\% \qquad\qquad (6)$$

Where N_c is the number of correctly classified samples, while N_t is the total number of samples. Even though DT can be easily applied, it has a serious overfitting problem. In many cases, DT performed well with training datasets but the opposite in real datasets due to outliers.

Random Forest (RF). RF classification was an elaborate method of DT as it is built on multiple DTs. The initial step to build an RF classifier was to perform bootstrapping. A subset of dimensions from each bootstrapped dataset will be used to compute a DT. The final output of an RF was determined by aggregating the outputs of all DTs. Data that was not involved in bootstrapping, known as an out-of-bag dataset, will be used to validate the performance of an RF classifier. By using multiple DTs, the sensitivity towards outliers was reduced and thus provided better performance.

Partial Least Square Regression (PLSR). The working principle of PLSR was to reduce many measured collinear spectral variables to a small amount of non-correlated latent variables or factors (Darvishzadeh et al., 2008). As a comparison with spectra, the latent variables were assumed to be the relevant information in the measured spectra and were used to calculate dependent variables, such as biophysical and biochemical characteristics. The final aim of PLSR was to build a linear model, as shown in Equation 7, used to classify data into two groups.

$$\Upsilon = X\beta + \varepsilon \qquad\qquad (7)$$

Where Y is a mean-centered vector of the dependent variable, X is a mean-centered matrix of independent variables (spectral bands in the study using HS image), β is a matrix of regression coefficients, and ε is a matrix of residuals. PLSR was like principal component regression (PCR), given that Equation 9 was used on latent variables of X. The difference was the decomposition of PLSR performed on both the spectra and responses simultaneously (Schlerf et al., 2003). A detailed description of PLSR can be reviewed by Geladi and Kowalski (1986).

Gaussian Process Regression (GPR). A joint multivariate normal distribution distributed the output values after GPR was applied. The mean vector of the joint distribution was generally assumed as zero vectors, and the covariance matrix was obtained using a covariance function defined over a pair of input values. Several works have successfully applied the GP regression to predict the biochemical characteristics from HS data (Arefi et al., 2021; Gewali & Monteiro, 2016). The details of the mathematical derivation of GPR were provided (Gewali et al., 2019).

Kernel Ridge Regression (KRR). KRR extends a simple linear regression by substituting the covariance with a kernel function (Mateo-García et al., 2018). The advantage of adopting KRR was its simplicity, as the aim is to find a parameter value that minimizes the mean square error. Besides, KRR was normally used when the training data was less as the computational cost was expensive for computing KRR for large datasets. The response for input x is estimated using KRR, as shown in Equation 8.

$$\overline{f}(x) = \sum_{j=1}^{n} k(x_j, x)\alpha_j \qquad (8)$$

Where given training data is $(x_1, y_1), \ldots, (x_n, y_n) \in \chi \times \gamma$, where $\chi \subseteq R^d$ is an input domain and $\gamma \subseteq R^d$ is an output domain. $\alpha = (\alpha_1 \ldots \alpha_n)^T$ is the solution of Equation 9.

$$(\chi^T \chi + \lambda I_n)\alpha = \chi^T \gamma \qquad (9)$$

Where λ is the regularization parameter > 0, $\chi^T \chi$ is the entries matrix, and γ is the vector responses. The KRR technique applied for the non-linear learning method for discrimination between healthy and stressed plants was demonstrated (Asaari et al., 2022).

Spectral Angle Mapper (SAM) classifier. The Spectral Angle Mapper (SAM) is a supervised classification that treats every spectrum as an *n-th* dimension vector in space. The angle between two spectra is computed using Equation 10 (Rashmi et al., 2014) to determine their similarity, where a smaller angle represents a higher similarity between two spectra.

$$\alpha = \cos^{-1}\left(\frac{\sum_{i=1}^{nb} t_i r_i}{\sqrt{\sum_{i=1}^{nb} t_i^2} \sqrt{\sum_{i=1}^{nb} r_i^2}} \right) \qquad (10)$$

Where *nb* is the number of bands, *t* is the spectrum vector, *r* is the reference spectrum vector, *and* α is the spectral angle. A distinct reference spectrum for each class is always required in HS analysis before SAM is applied.

Table 1
List of image acquisition criteria focuses on proximal HSI analysis on crop

Imaging Method	Imaging Condition	Camera Model Name	Spectrum Wavelength	Wavelength Interval	Light Source	Imaging Subject	Authors
Pushbroom	Indoor	ImSpector V10E	400–1000 nm	~ 3 nm	15W tungsten halogen light	Potato plants	Mishra, Polder et al., 2020
					Combination of 105W halogen lamp and 56W LED	Apple slices	Arefi et al., 2021
					Two 3x3 35W halogen lamps	Maize plants	Mohd Asaari et al., 2018
					150W halogen lamp	Wheat plants	Bauriegel et al., 2011
					Two lightlines for homogenous illumination	Sugar beet leaves	Leucker et al., 2016
					Two linear light emitters	Barley leaves	Kuska et al., 2015
					150W fiber halogen lamp	Cucumber downy mildew leaves	Tian & Zhang, 2012
		ImSpector V10E + N25E	400–2500 nm	Not specified	Not specified	Sugar beet leaves	Behmann et al., 2016
		Specim V9 Spectrograph	460–900 nm	7 nm	Incandescent light and two 150W halogen lamps	Wheat plants	Moshou et al., 2014
		Gaia Hyperspectral Camera V10E	862.9–1704.2 nm	2.8 nm	Not specified	Potato plants leaves	Sun et al., 2018
		SisuCHEMA Imaging System	1000–2500 nm	6.5 nm	Not specified	Maize kernels	Manley et al., 2009
		Headwall Photonics Spectrometer	550–1700 nm	4.7 nm	Two 35W halogen lamps	Maize plants and soybean plants	Pandey et al., 2017
		FSR Hyperspectral Camera	400–1000 nm	Not specified	10W tungsten halogen lamp	Cucumber leaves	Sabzi et al., 2021
		Innspector N17E-OWL320	900–1700 nm	5 nm	Two 150W halogen lamps	Chinese congou black tea	Ren et al., 2020
		Surface Optics Corp - 700	400–900 nm	4 nm	Six 400W halogen lamps	Barley and corn plants	Romer et al., 2012

Table 1 *(continue)*

Imaging Method	Imaging Condition	Camera Model Name	Spectrum Wavelength	Wavelength Interval	Light Source	Imaging Subject	Authors
		iXon Imaging Device	450–920 nm	2.8 nm	Two 150W halogen lamps	Ruby red grapefruit	Qin et al., 2009
	Outdoor	HySpex VNIR 1600-160	400–1000 nm	3.7 nm	Sunlight	Wheat plants, wheat leaves, and wheat field	Vigneau et al., 2011
		Specim IQ Sensor	397–1004 nm	3 nm	Sunlight	Vines	Nguyen et al., 2021
Snapshot	Indoor	Hyperspectral Snapshot Mosaic Camera	470–1000 nm	12 nm	Four 50W halogen lamps	Maize seeds	Gao et al., 2018
Not specified	Indoor	ASD Fieldspec FR Spectrometer	350–2500 nm	3nm and 10nm below and above 1000nm, respectively	100W halogen reflector	Sugar beet leaves	Mahlein et al., 2010
					Not specified	Corn leaves	Sun et al., 2021
					Not specified	Rice crops	Wang et al., 2010
					100W halogen lamp	Sugar beet leaves	Rumpf et al., 2010
					50W halogen lamp	Rice crop leaves	Liu et al., 2007
		Unispec PP Systems	350–1100 nm	3.5 nm	Halogen lamp	Leaf from different species	Sims & Gamon, 2002
		FieldSpec UV/VNIR Spectroradiometer	350–1050 nm	3 nm	Li-1800 integrating sphere	Winter wheat leaves	Yuan et al., 2014; J. Zhang et al., 2012
		SVC HR-1024 Spectroradiometer	350–1000 nm	3.5 nm	Two 500W halogen lamps	Avocado plant leaves	Sankaran et al., 2012
	Outdoor	ASD Fieldspec FR Spectrometer	350–2500 nm	3nm and 10nm below and above 1000nm, respectively	Sunlight	Winter wheat	Fu et al., 2014
						Maize plants	Zhang & Zhou, 2019
						Celery crop	Huang & Apan, 2006
						Palmar amaranth and cotton seeds	Fletcher & Turley, 2017
		GER 1500 spectrometer	300–1100 nm	1.55 nm	Sunlight	Rice crop	Nguyen & Lee, 2006

Table 2

List of illumination correction, feature extraction, and spectral modeling focus on proximal HSI analysis on crop

Illumination Correction	Feature Extraction	Spectral Modelling	Authors
Average	Not specified	PLSR, PCR	Liu et al., 2007
	Not specified	PLSR	Ge et al., 2016 Pandey et al., 2017
SNV	ANOVA	K-means, Computation of ED	Asaari et al., 2018)
	ANOVA	SVM + K-means	Asaari et al., 2019
	Not specified	PLSR	Nguyen & Lee, 2006 Vigneau et al., 2011
	Not specified	ANN	Sabzi et al., 2021
MSC	PCA	DT	Ren et al., 2020
Spectral Smoothing	Competitive Adaptive Reweighted Sampling (CARS)	PLSR	Sun et al., 2021
Derivatives	Not specified	PLSR	Huang & Apan, 2006 Fu et al., 2014
		Spectral Angle Mapper (SAM)	Leucker et al., 2016
		RF	Fletcher & Turley, 2017
MSC + SNV	PCA	PLS-DA	Manley et al., 2009
VSN + SNV	Not specified	K-means clustering	Mishra, Polder et al., 2020
MSC + Spectral Smoothing	Neighborhood Component Analysis (NCA), PLSR	GPR, Bagging Decision Tree (BDT), Lasso Regression	Arefi et al., 2021
Not specified	PCA	SVM, RF	Nguyen et al., 2021
	PCA	RF, KNN	Gao et al., 2018
	CA, CARS	PLSR	Sun et al., 2018
	ANOVA	Computation of VIs	Mahlein et al., 2010
	Not specified	SVM, least square SVM, MLP	Moshou et al., 2014

UTILIZATION OF SPATIAL INFORMATION

Each pixel of the HS image was formed by a spectral vector, which consists of multiple bands. Undeniably, many plant traits can be observed by utilizing spectral information alone. However, spatial information should not be overlooked to explore the potential of HS images fully. The spatial information can be from the HS image or obtained from other sensors, commonly the depth sensor. Table 3 summarizes the research works that utilized spatial images in proximal HS analysis.

Foreground-Background Segmentation

The purpose of foreground-background segmentation in HS images was to remove the pixels not part of the sample under investigation. This approach was used to remove

unwanted background by calculating the NDVI value of each pixel (Asaari et al., 2018; Behmann et al., 2014; Pandey et al., 2017). This method might not be efficient if the background consists of an object that reflected illumination within the NIR or red range.

The background removal performed by using NDVI could be improved by analyzing spatial information to eliminate the remaining pixels that were not part of the sample plant. Williams et al. (2017) eroded the HS image using a 3×3 cross-shaped structural element to remove stray and mixed pixels at the leaf's edge after the NDVI segmentation step. The image erosion determined if a particular pixel belonged to the sample plant via its neighboring pixels. If most neighboring pixels were the plant's pixel, the target pixel would be set to the plant pixel and vice versa. Besides, a graph theory that required a low computational power was also implemented to segmentize the sample from a background that reflected a similar intensity of VNIR illumination as a sample.

Chen et al. (2019) explored object segmentation using the HS lidar sensor system. Nine different materials were aimed to be segmented via 3D point clouds obtained using the lidar sensor. The obtained 3D data were processed using connected-component labeling (CCL), a point cloud segmentation method that did not require a seed point. It was initially used in binary digital images by isolating components that did not overlap spatially, whereby points in each component had similar properties. The same theory could be applied when segmenting objects in a 3D point cloud and sample plant from its background, which had different spectral properties.

Noise Reduction and Morphological Profile

Different kinds of noise can degrade the HS image quality. Huang et al. (2021) set input data within a certain range by comparing it with white and dark references to reduce the effect of noise. Kool et al. (2021) implemented morphological closing to remove noise before the classification. Morphological closing involved a dilation followed by erosion to remove gaps caused by noise. It allowed the noisy pixels to be corrected and used for consequent processing steps.

Morphological profile (MP) is obtained by opening and closing the original image. Small bright pixels could be eliminated by opening, while small dark pixels could be eliminated by closing. Different MPs could be obtained depending on the scale and structural element (SE) that came in different shapes like disk-shaped, linear-shaped, cross-shaped, and so on, depending on the shape that wishes to be removed. MPs were generated by exploring the spatial information of HS images (Liao et al., 2019; Villegas et al., 2017). The MPs were combined with the first few principal components (PCs) for further analysis. Both studies showed that the fusion of MPs and PCs performed better than just utilizing solely spectral information for analysis.

Point Clouds for HS 3D Model

During image acquisition, the reflected illumination was not always towards the camera due to the inclined normal of the complex geometry of the plant. It caused an illumination effect as the reflected illumination might overlap before reaching the camera. In most studies utilizing only spectral data, the spectral information would be corrected with mathematical formulas, such as spectral averaging, standard normal variation (SNV), and variable sorting normalization (VSN), and were able to improve the analysis accuracy to a certain extent. However, modeling the scattering effect of illumination was dependent on the leaves' inclination angle and precise estimation of the inclination angle of every leaf, whereby using spectral information alone was nearly impossible.

One of the promising solutions for this issue was combining spatial and spectral information by using 3D point clouds of HS images. 3D point clouds were generated using different depth sensors and incorporated with HS information for analysis (Behmann et al., 2016; Huang et al., 2018; Villegas et al., 2017). The inclination angle of leaves could be computed with 3D models, reducing the illumination effect. The studies proved that the analysis accuracy was higher by fusing geometry information with the original HS information than by solely analyzing the spectral information. Even though incorporating 3D models provided better analysis results, it did not come without disadvantages. One of the concerns when using this method was the additional requirement of a depth sensor. Besides, acquiring accurate 3D point clouds required precise calibration and more time.

Deep Learning for HS Image Classification

Deep learning utilized the spectral and spatial information of HS images and outperformed the conventional machine learning method in many situations. For instance, Yan et al. (2021) compared the convolutional neural network (CNN) with conventional machine learning methods like logistic regression (LR), standard vector machine (SVM), neural network (NN), and decision tree (DT) on 1D, 2D and 3D data extracted from HS images. The results showed that CNN had the highest accuracy when used on first derivative spectra and HS images to detect the existence of aphids in cotton. Whereas for RGB images (2D), CNN achieved the same accuracy as LR, which was also one of the highest of all five methods.

Deep learning usually refers to a deep neural network consisting of a recurrent neural network (RNN), CNN, and generative adversarial network (GAN). These methods were called 'deep' as data would be processed in many layers, each performing a different function. Amongst various deep neural networks, CNN is the most popular network for image and speech recognition due to its strength in extracting features from complex data. Even though CNN has shown great potential for complex data analysis, it is not completely free from limitations. One of the concerns when implementing CNN to study plant traits is the limited number of samples used for training (Paoletti et al., 2018).

Besides, the limited samples coupled with high data dimensionality also led to another problem, commonly referred to as the Hughes phenomenon, also known as the curse of dimensionality (Khodadadzadeh et al., 2014).

In recent studies, augmented data to tackle a limited number of samples (Z. Wang et al., 2018; Zhao et al., 2021). Techniques for data augmentation include flipping horizontally and vertically and randomly rotating the image quarterly. Besides, Nagasubramanian et al. (2019) cropped the original HS images spatially random into fixed smaller sample sizes to increase the number of training samples. The augmented data generated by these techniques would appear as different inputs to the neural network, as deep learning is a spectral-spatial-based analysis method. As shown in Figure 6, the conventional architecture of CNN can be classified into two parts: the feature learning layer and the classification layer. Feature learning layers consist of convolutional layers, pooling layers, batch normalization, and activation functions. On the other hand, the classification layer is formed by fully connected layers.
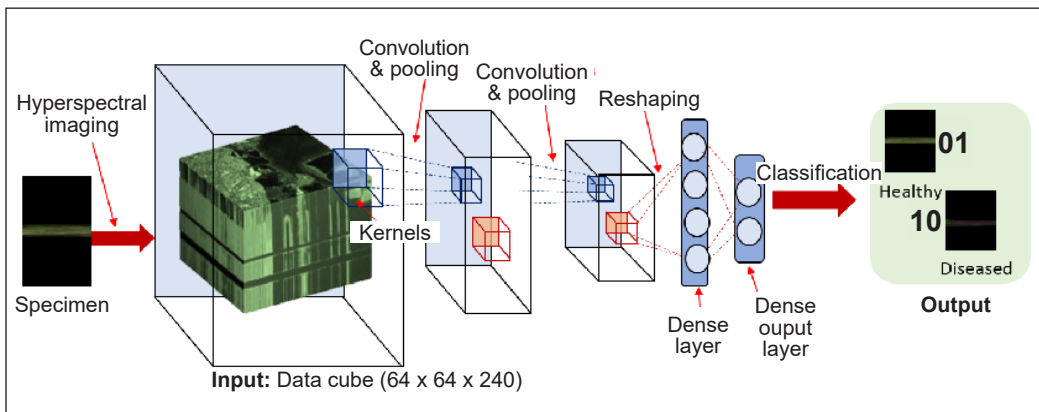

Figure 6. Conventional architecture of CNN of HSI

When pre-processing data is fed into CNN for training, it initially goes through the convolutional layer. If the data is an RGB image, a 2D convolutional kernel would be used to convolute the image so that features like edges, vertices, lines, and so on would be extracted. For the case of HS images, a 3D convolutional kernel would be used to extract spectral-spatial features. The work presented by Nagasubramanian et al. (2019) and Nguyen et al. (2021) used $3\times3\times3$ used $3\times3\times3$ and $3\times3\times16$ pixels kernels, respectively, in all five methods and two convolutional layers. The size of the kernel could affect the model's accuracy. Larger kernels tend to capture high-resolution patterns with the downside of more parameters and computational power. However, the model performance was not proportional to kernel size. The accuracy of the model would drop when the kernel size exceeds a certain threshold. Tan and Le (2020) suggested mixing large and small kernels to capture high- and low-resolution patterns.

Each convolutional layer is normally followed by a batch normalization layer and a pooling layer (Nguyen et al., 2021; Yan et al., 2021, 2019). The purpose of batch normalization is to reduce internal shift, which is the change in network activation distributions due to network parameters change during training (Ioffe & Szegedy, 2015). By doing this, the issue of unstable gradient can be addressed, and the learning rate can be increased. The layer that ensues is the pooling layer, which helps prevent overfitting and reduce the complexity of the network, thus lowering the computational cost. Types of pooling layers are max pooling and average pooling. When the pooling layer is applied to 3D data, the height and width are reduced, but the depth remains unchanged.

Since the output value from every layer is not bounded, a large value might lead to computational issues for the model as the layer gets deeper. The activation function is applied to set the input within a certain range after every layer, normally after the pooling layer in CNN. Besides, the activation function adds non-linearity to a neural network. For example, Equation 11 shows layers of functions stacked within each other. This forms non-linearity, which allows the model to learn patterns from a complex dataset. $fn(x)$ can be any non-linear activation function like rectified linear unit (ReLU), Sigmoid, or SoftMax function, represented in Equations 12, 13, and 14, respectively. ReLU is commonly used at the current stage as it requires the least computational costs.

$$o(x) = f_n\left(f_{n-1}\left(\ldots f_1(x)\right)\right) \tag{11}$$

$$f(x) = \max(0, x) \tag{12}$$

$$f(x) = \frac{1}{1+e^{-x}} \tag{13}$$

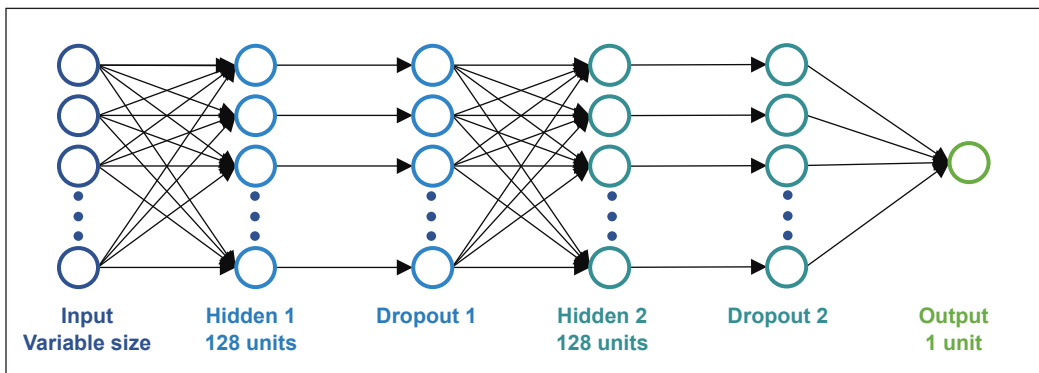$$f(x_i) = \frac{e^{x_i}}{\sum_0^j x_j} \tag{14}$$

Figure 7. Conventional architecture of fully connected layer (Sun et al., 2019)

The convolutional layer serves as a feature extraction function to work with other ML methods, as demonstrated by Nguyen et al. (2021). In many studies, data after convolutional layers are flattened to a 1D vector and fed into a fully connected layer, also known as a dense layer, in which inputs and outputs are related via learnable weight. Figure 7 shows the conventional architecture with 2 hidden and 2 dropout layers. The dropout layer helps to prevent model overfitting and is used only during training. However, information loss might occur when the parameter of the dropout layer is not correctly set.

Table 3
List of studies that utilize spatial images in close-range HSI analysis

Spatial Information Use Case	Spectrum Wavelength	Wavelength Interval	Research Subject	Authors
Combine 3D models with HS images to remove geometry-related effects in HS analysis	400–2500 nm	Not specified	Sugar beets	**Behmann et al., 2016**
	400–1000 nm	7 nm	Aagrow soybean	**Huang et al., 2018**
	380–2200 nm	4.69 nm	Tomato palnts	**Sun et al., 2019**
Analyse 3D HS image using CNN, which preserves spectral and spatial information	376–1044 nm	5 nm	Cotton leaves	**Yan et al., 2021**
	328.81–1113.54 nm	0.78 nm	Blueberry	**Wang, Hu et al., 2018**
	400–1000 nm	2.5 nm	Glycine max (L.) Merr. soybean	**Nagasubramanian et al., 2019**
	397–1004 nm	3 nm	Grapevines	**Nguyen et al., 2021**
Compute mean spectral reflectance from spatially selected ROIs	395–885 nm	2.05 nm	Corn seedlings	**Yang et al., 2019**
	450–950 nm	3.97 nm	Cotton	**Zhao et al., 2021**
Morphological process to remove noise spatially	467–900 nm	2.87 nm	Potato plants	**Kool et al., 2021**
	400–2506nm	1.23 nm and 5.79 nm for below and above 895, respectively	Gien Moy and Latham raspberries	**Williams et al., 2017**
Generate MPs to support processes like noise removal and combination with PCs	364–1031 nm	4.5 nm	Banana leaves	**Liao et al., 2019**
	364–1031 nm	4.5 nm	Banana leaves	**Villegas et al., 2017**
Classification of objects with different material properties in 3D data via CCL	500–820 nm	9.69 nm	Peperomia tetraphylla plant, Sansevieria Trifasciata plant, and other non-living objects	**Chen et al., 2019**

REMAINING TECHNICAL CHALLENGES

Even though HS image carries a large amount of information, researchers still faced many challenges during the studies. Each stage poses certain difficulties that need to be tackled before a study is carried out. For instance, the inconsistent natural light makes outdoor data

acquisition more difficult. Therefore, factors like weather forecasts must be considered prior to data acquisition.

Even though the HS camera is decreasing, it is still costly compared to imaging devices like thermal and RGB because the HS camera is still mainly used for research purposes, and there are fewer providers for such cameras. It makes HS a niche device that can hardly be obtained.

Every pixel of an HS image is a vector of spectra information. Unlike RGB images with three bands or multispectral images with 10-20 bands, the pixel vector of HS images can be hundreds of elements long. It leads to costly storage for HS images. Besides, remote data transfer for such a huge amount of data is challenging. One possible solution is to use a compression algorithm where no data loss occurs when compressed data is extracted.

One of the challenges with deep learning adoption for HS analysis is that the amount of training dataset is still insufficient in many studies because the public HS dataset is fewer, and the datasets required are specific, depending on the subject studied. The common approach is via data augmentation, whereby the available training dataset is rotated, scaled, cropped, and added noise to assemble the subject under different conditions.

CONCLUSION

HS image carries much information both spectrally and spatially. In many cases, spatial information is used only in pre-processing steps like segmentation and noise reduction. For model training, the use case of HS spectral-spatial information is demonstrated by deep learning. In many studies, CNN showed better performance as compared to the conventional pixel-based analysis, which treats every pixel independently. Therefore, deep learning methods utilizing spectral and spatial information should be the research focus in future HSI analysis to derive full benefits from HS information.

Besides, one piece of information that can hardly be explored and utilized from HS images is the pixel depth. The depth information is usually provided using an external depth sensor. Currently, most studies about neural network analysis on proximal HSI do not include in-depth information. Hence, there is potential to integrate depth information with HS images trained by neural networks to improve accuracy in studying plant traits.

ACKNOWLEDGEMENT

REFERENCES

Arefi, A., Sturm, B., von Gersdorff, G., Nasirahmadi, A., & Hensel, O. (2021). Vis-NIR hyperspectral imaging along with Gaussian process regression to monitor quality attributes of apple slices during drying. *LWT*, *152*, Article 112297. https://doi.org/10.1016/j.lwt.2021.112297

Asaari, M. S. M., Mertens, S., Dhondt, S., Inzé, D., & Scheunders, P. (2022). Analysis of plant stress response using hyperspectral imaging and kernel ridge regression. In N. M. Mahyuddin, N. R. M. Noor & H. A. M. Sakim (Eds.), *Proceedings of the 11th Internationl Conference on Robotics, Vision, Signal Processing and Power Application* (pp. 426-431). Springer. https://doi.org/10.1007/978-981-16-8129-5_66

Asaari, M. S. M., Mertens, S., Dhondt, S., Inzé, D., Wuyts, N., & Scheunders, P. (2019). Analysis of hyperspectral images for detection of drought stress and recovery in maize plants in a high-throughput phenotyping platform. *Computers and Electronics in Agriculture, 162*, 749-758. https://doi.org/10.1016/j.compag.2019.05.018

Asaari, M. S. M., Mishra, P., Mertens, S., Dhondt, S., Inzé, D., Wuyts, N., & Scheunders, P. (2018). Close-range hyperspectral image analysis for the early detection of stress responses in individual plants in a high-throughput phenotyping platform. *ISPRS Journal of Photogrammetry and Remote Sensing, 138*, 121-138. https://doi.org/10.1016/j.isprsjprs.2018.02.003

Bauriegel, E., Giebel, A., Geyer, M., Schmidt, U., & Herppich, W. B. (2011). Early detection of Fusarium infection in wheat using hyper-spectral imaging. *Computers and Electronics in Agriculture, 75*(2), 304-312. https://doi.org/10.1016/j.compag.2010.12.006

Behmann, J., Mahlein, A. K., Paulus, S., Dupuis, J., Kuhlmann, H., Oerke, E. C., & Plümer, L. (2016). Generation and application of hyperspectral 3D plant models: Methods and challenges. *Machine Vision and Applications, 27*(5), 611-624. https://doi.org/10.1007/s00138-015-0716-8

Behmann, J., Steinrücken, J., & Plümer, L. (2014). Detection of early plant stress responses in hyperspectral images. *ISPRS Journal of Photogrammetry and Remote Sensing, 93*, 98-111. https://doi.org/10.1016/j.isprsjprs.2014.03.016

Bradley, P. E., Keller, S., & Weinmann, M. (2018). Unsupervised feature selection based on ultrametricity and sparse training data: A case study for the classification of high-dimensional hyperspectral data. *Remote Sensing*, *10*(10), Article 1564. https://doi.org/10.3390/rs10101564

Brownson, J. R. S. (2014). *Solar Energy Conversion Systems*. Elsevier Inc. https://doi.org/https://doi.org/10.1016/C2011-0-07039-4

Chen, B., Shi, S., Sun, J., Gong, W., Yang, J., Du, L., Guo, K., Wang, B., & Chen, B. (2019). Hyperspectral lidar point cloud segmentation based on geometric and spectral information. *Optics Express, 27*(17), 24043-24059. https://doi.org/10.1364/oe.27.024043

Darvishzadeh, R., Skidmore, A., Schlerf, M., Atzberger, C., Corsi, F., & Cho, M. (2008). LAI and chlorophyll estimation for a heterogeneous grassland using hyperspectral measurements. *ISPRS Journal of Photogrammetry and Remote Sensing, 63*(4), 409-426. https://doi.org/10.1016/j.isprsjprs.2008.01.001

Dinç, S., & Aygün, R. S. (2013). Evaluation of hyperspectral image classification using random forest and Fukunaga-Koontz transform. In P. Perner (Ed.), *Machine Learning and Data Mining in Pattern Recognition* (pp. 234-245). Springer. https://doi.org/10.1007/978-3-642-39712-7_18

Elmasry, G., Kamruzzaman, M., Sun, D. W., & Allen, P. (2012). Principles and applications of hyperspectral imaging in quality evaluation of agro-food products: A review. *Critical Reviews in Food Science and Nutrition, 52*(11), 999-1023. https://doi.org/10.1080/10408398.2010.543495

Fischler, M. A., & Bolles, R. C. (1987). Random sample consensus: A paradigm for model fitting with applications to image analysis and automated cartography. In M. A. Fischler & O. Firschein (Eds.), *Readings in Computer Vision* (pp. 726-740). Morgan Kaufmann Publishers, Inc. https://doi.org/10.1016/b978-0-08-051581-6.50070-2

Fletcher, R. S., & Turley, R. B. (2017). Employing canopy hyperspectral narrowband data and random forest algorithm to differentiate palmer amaranth from colored cotton. *American Journal of Plant Sciences, 08*(12), 3258-3271. https://doi.org/10.4236/ajps.2017.812219

Fu, Y., Yang, G., Wang, J., Song, X., & Feng, H. (2014). Winter wheat biomass estimation based on spectral indices, band depth analysis and partial least squares regression using hyperspectral measurements. *Computers and Electronics in Agriculture, 100*, 51-59. https://doi.org/10.1016/j.compag.2013.10.010

Gao, J., Nuyttens, D., Lootens, P., He, Y., & Pieters, J. G. (2018). Recognising weeds in a maize crop using a random forest machine-learning algorithm and near-infrared snapshot mosaic hyperspectral imagery. *Biosystems Engineering, 170*, 39-50. https://doi.org/10.1016/j.biosystemseng.2018.03.006

Ge, Y., Bai, G., Stoerger, V., & Schnable, J. C. (2016). Temporal dynamics of maize plant growth, water use, and leaf water content using automated high throughput RGB and hyperspectral imaging. *Computers and Electronics in Agriculture, 127*, 625-632. https://doi.org/10.1016/j.compag.2016.07.028

Geladi, P., & Kowalski, B. R. (1986). Partial least-squares regression: A tutorial. *Analytica Chimica Acta*, *185*, 1-17. https://doi.org/10.1016/0003-2670(86)80028-9

Gewali, U. B., & Monteiro, S. T. (2016, September 25-28). *A novel covariance function for predicting vegetation biochemistry from hyperspectral imagery with Gaussian processes*. [Paper presentation]. International Conference on Image Processing (ICIP), Arizona, USA. https://doi.org/10.1109/ICIP.2016.7532752

Gewali, U. B., Monteiro, S. T., & Saber, E. (2019). Gaussian processes for vegetation parameter estimation from hyperspectral data with limited ground truth. *Remote Sensing, 11*(13), Article 1614. https://doi.org/10.3390/rs11131614

Goetz, A. F. H. (2009). Three decades of hyperspectral remote sensing of the Earth: A personal view. *Remote Sensing of Environment, 113*(SUPPL. 1), S5-S16. https://doi.org/10.1016/j.rse.2007.12.014

Gonzalez, R. C., & Woods, R. E. (1993). *Digital Image Processing* (3rd ed.). Pearson.

Grönwall, C., Steinvall, O., Göhler, B., & Hamoir, D. (2016). Active and passive imaging of clothes in the NIR and SWIR regions for reflectivity analysis. *Applied Optics, 55*(20), Article 5292. https://doi.org/10.1364/ao.55.005292

Guo, Y., Yin, X., Zhao, X., Yang, D., & Bai, Y. (2019). Hyperspectral image classification with SVM and guided filter. *Eurasip Journal on Wireless Communications and Networking, 2019*(1), 1-9. https://doi.org/10.1186/s13638-019-1346-z

Gupta, N., Dahmanja, R., Gottliebb, M., Denes, L., Kaminsky, B., & Metes, P. (1999). Hyperspectral imaging using acousto-optic tunable filters. *Proceedings AEROSENSE, 3718*, 512-521. https://doi.org/10.1117/12.359988

Huang, J. F., & Apan, A. (2006). Detection of sclerotinia rot disease on celery using hyperspectral data and partial least squares regression. *Journal of Spatial Science, 51*(2), 129-142. https://doi.org/10.1080/14498596.2006.9635087

Huang, P., Luo, X., Jin, J., Wang, L., Zhang, L., Liu, J., & Zhang, Z. (2018). Improving high-throughput phenotyping using fusion of close-range hyperspectral camera and low-cost depth sensor. *Sensors, 18*(8), Article 2711. https://doi.org/10.3390/s18082711

Huang, Y., Li, J., Yang, R., Wang, F., Li, Y., Zhang, S., Wan, F., Qiao, X., & Qian, W. (2021). Hyperspectral imaging for identification of an invasive plant mikania micrantha kunth. *Frontiers in Plant Science, 12*, Article 626516. https://doi.org/10.3389/fpls.2021.626516

Ioffe, S., & Szegedy, C. (2015, July 6-11). *Batch normalization: Accelerating deep network training by reducing internal covariate shift*. [Paper presentation]. 32nd International Conference on Machine Learning (ICML), Lille, France.

Khodadadzadeh, M., Li, J., Plaza, A., Ghassemian, H., Bioucas-Dias, J. M., & Li, X. (2014). Spectral-spatial classification of hyperspectral data using local and global probabilities for mixed pixel characterization. *IEEE Transactions on Geoscience and Remote Sensing, 52*(10), 6298-6314. https://doi.org/10.1109/TGRS.2013.2296031

Kool, J., Been, T., & Evenhuis, A. (2021, March 24-26). *Detection of latent potato late blight by hyperspectral imaging*. [Paper presentation]. 11th Workshop on Hyperspectral Image and Signal Processing, Evolution in Remote Sensing, Amsterdam, Netherlands. https://doi.org/10.1109/WHISPERS52202.2021.9484002

Kuska, M., Wahabzada, M., Leucker, M., Dehne, H. W., Kersting, K., Oerke, E. C., Steiner, U., & Mahlein, A. K. (2015). Hyperspectral phenotyping on the microscopic scale: Towards automated characterization of plant-pathogen interactions. *Plant Methods, 11*(1), Article 28. https://doi.org/10.1186/s13007-015-0073-7

Leucker, M., Mahlein, A. K., Steiner, U., & Oerke, E. C. (2016). Improvement of lesion phenotyping in cercospora beticolasugar beet interaction by hyperspectral imaging. *Phytopathology, 106*(2), 177-184. https://doi.org/10.1094/PHYTO-04-15-0100-R

Li, L., Zhang, Q., & Huang, D. (2014). A review of imaging techniques for plant phenotyping. *Sensors, 14*(11), 20078-20111. https://doi.org/10.3390/s141120078

Liao, W., Ochoa, D., Gao, L., Zhang, B., & Philips, W. (2019, July 29- August 2). *Morphological analysis for banana disease detection in close range hyperspectral remote sensing images*. [Paper presentation]. IEEE International Symposium on Geoscience and Remote Sensing (IGARSS), Yokohama, Japan. https://doi.org/10.1109/IGARSS.2019.8899087

Liu, Z. Y., Huang, J. F., Shi, J. J., Tao, R. X., Zhou, W., & Zhang, L. L. (2007). Characterizing and estimating rice brown spot disease severity using stepwise regression, principal component regression and partial least-square regression. *Journal of Zhejiang University Science B, 8*(10), 738-744. https://doi.org/10.1631/jzus.2007.B0738

Lu, B., Dao, P. D., Liu, J., He, Y., & Shang, J. (2020). Recent advances of hyperspectral imaging technology and applications in agriculture. *Remote Sensing, 12*(16), 1-44. https://doi.org/10.3390/RS12162659

Luo, G., Chen, G., Tian, L., Qin, K., & Qian, S. E. (2016). Minimum noise fraction versus principal component analysis as a preprocessing step for hyperspectral imagery denoising. *Canadian Journal of Remote Sensing, 42*(2), 106-116. https://doi.org/10.1080/07038992.2016.1160772

Mahlein, A. K., Steiner, U., Dehne, H. W., & Oerke, E. C. (2010). Spectral signatures of sugar beet leaves for the detection and differentiation of diseases. *Precision Agriculture, 11*(4), 413-431. https://doi.org/10.1007/s11119-010-9180-7

Manley, M., Williams, P., Nilsson, D., & Geladi, P. (2009). Near infrared hyperspectral imaging for the evaluation of endosperm texture in whole yellow maize (*Zea maize* L.) Kernels. *Journal of Agricultural and Food Chemistry, 57*(19), 8761-8769. https://doi.org/10.1021/jf9018323

Mateo-García, G., Laparra, V., & Gómez-Chova, L. (2018, July 22-27). *Optimizing kernel ridge regression for remote sensing problems*. [Paper presentation]. IEEE International Symposium on Geoscience and Remote Sensing (IGARSS), Velencia, Spain. https://doi.org/10.1109/IGARSS.2018.8518016

Mishra, P., Lohumi, S., Ahmad Khan, H., & Nordon, A. (2020). Close-range hyperspectral imaging of whole plants for digital phenotyping: Recent applications and illumination correction approaches. *Computers and Electronics in Agriculture, 178*, Article 105780. https://doi.org/10.1016/j.compag.2020.105780

Mishra, P., Polder, G., Gowen, A., Rutledge, D. N., & Roger, J. M. (2020). Utilising variable sorting for normalisation to correct illumination effects in close-range spectral images of potato plants. *Biosystems Engineering, 197*, 318-323. https://doi.org/10.1016/j.biosystemseng.2020.07.010

Moshou, D., Pantazi, X. E., Kateris, D., & Gravalos, I. (2014). Water stress detection based on optical multisensor fusion with a least squares support vector machine classifier. *Biosystems Engineering, 117*(1), 15–22. https://doi.org/10.1016/j.biosystemseng.2013.07.008

Moughal, T. A. (2013). Hyperspectral image classification using support vector machine. *Journal of Physics: Conference Series, 439*(1), Article 012042. https://doi.org/10.1088/1742-6596/439/1/012042

Nagasubramanian, K., Jones, S., Singh, A. K., Sarkar, S., Singh, A., & Ganapathysubramanian, B. (2019). Plant disease identification using explainable 3D deep learning on hyperspectral images. *Plant Methods, 15*(1), 1-10. https://doi.org/10.1186/s13007-019-0479-8

Nguyen, C., Sagan, V., Maimaitiyiming, M., Maimaitijiang, M., Bhadra, S., & Kwasniewski, M. T. (2021). Early detection of plant viral disease using hyperspectral imaging and deep learning. *Sensors, 21*(3), Article 742. https://doi.org/10.3390/s21030742

Nguyen, H. T., & Lee, B. (2006). Assessment of rice leaf growth and nitrogen status by hyperspectral canopy reflectance and partial least square regression. *European Journal of Agronomy, 24*(4), 349-356. https://doi.org/10.1016/j.eja.2006.01.001

Nielsen, A. A. (2011). Kernel maximum autocorrelation factor and minimum noise fraction transformations. *IEEE Transactions on Image Processing, 20*(3), 612-624. https://doi.org/10.1109/TIP.2010.2076296

Pandey, P., Ge, Y., Stoerger, V., & Schnable, J. C. (2017). High throughput in vivo analysis of plant leaf chemical properties using hyperspectral imaging. *Frontiers in Plant Science, 8*(1348), 1-12. https://doi.org/10.3389/fpls.2017.01348

Paoletti, M. E., Haut, J. M., Plaza, J., & Plaza, A. (2018). A new deep convolutional neural network for fast hyperspectral image classification. *ISPRS Journal of Photogrammetry and Remote Sensing, 145*(Part A), 120-147. https://doi.org/10.1016/j.isprsjprs.2017.11.021

Paulus, S., & Mahlein, A. K. (2020). Technical workflows for hyperspectral plant image assessment and processing on the greenhouse and laboratory scale. *GigaScience, 9*(8), 1-10. https://doi.org/10.1093/gigascience/giaa090

Qin, J., Burks, T. F., Ritenour, M. A., & Bonn, W. G. (2009). Detection of citrus canker using hyperspectral reflectance imaging with spectral information divergence. *Journal of Food Engineering, 93*(2), 183-191. https://doi.org/10.1016/j.jfoodeng.2009.01.014

Ray, D. K., Mueller, N. D., West, P. C., & Foley, J. A. (2013). Yield trends are insufficient to double global crop production by 2050. *PloS One, 8*(6), Article e66428. https://doi.org/10.1371/journal.pone.0066428

Ren, G., Wang, Y., Ning, J., & Zhang, Z. (2020). Using near-infrared hyperspectral imaging with multiple decision tree methods to delineate black tea quality. *Spectrochimica Acta - Part A: Molecular and Biomolecular Spectroscopy, 237*, Article 118407. https://doi.org/10.1016/j.saa.2020.118407

Rodarmel, C., & Shan, J. (2002). Principal component analysis for hyperspectral image classification. *Surveying and Land Information Science, 62*(2), 115-122.

Romer, C., Wahabzada M., Ballvora A., Pinto, F., Rossini, M., Panigada, C., Behmann, J., Leon, J., Thurau, C., Bauckhage, C., Kersting, K., Rascher, U., & Plumer, L. (2012). Early drought stress detection in cereals: Simplex volume maximisation for hyperspectral image analysis. *Functional Plant Biology, 39*(11), 878-890. https://doi.org/10.1071/FP12060

Rumpf, T., Mahlein, A. K., Steiner, U., Oerke, E. C., Dehne, H. W., & Plümer, L. (2010). Early detection and classification of plant diseases with support vector machines based on hyperspectral reflectance. *Computers and Electronics in Agriculture, 74*(1), 91-99. https://doi.org/10.1016/j.compag.2010.06.009

Sabzi, S., Pourdarbani, R., Rohban, M. H., García-Mateos, G., Paliwal, J., & Molina-Martínez, J. M. (2021). Early detection of excess nitrogen consumption in cucumber plants using hyperspectral imaging based on hybrid neural networks and the imperialist competitive algorithm. *Agronomy, 11*(3), Article 575. https://doi.org/10.3390/agronomy11030575

Saha, D., & Manickavasagan, A. (2021). Machine learning techniques for analysis of hyperspectral images to determine quality of food products: A review. *Current Research in Food Science, 4*, 28-44. https://doi.org/10.1016/j.crfs.2021.01.002

Salazar-vazquez, J., & Mendez-vazquez, A. (2020). HardwareX A plug-and-play Hyperspectral Imaging Sensor using low-cost equipment. *HardwareX, 7*, Article e00087. https://doi.org/10.1016/j.ohx.2019.e00087

Sankaran, S., Ehsani, R., Inch, S. A., & Ploetz, R. C. (2012). Evaluation of visible-near infrared reflectance spectra of avocado leaves as a non-destructive sensing tool for detection of laurel wilt. *Plant Disease, 96*(11), 1683-1689. https://doi.org/10.1094/PDIS-01-12-0030-RE

Schlerf, M., Atzberger, C., Udelhoven, T., Jarmer, T., Mader, S., Werner, W., & Hill, J. (2003, May 13-16). *Spectrometric estimation of leaf pigments in Norway spruce needles using band-depth analysis, partial least-square regression and inversion of a conifer leaf model*. [Paper presentation]. 3rd EARSeL Workshop on Imaging Spectroscopy, Herrsching, Germany.

Sims, D. A., & Gamon, J. A. (2002). Relationships between leaf pigment content and spectral reflectance across a wide range of species, leaf structures and developmental stages. *Remote Sensing of Environment, 81*(2-3), 337-354. https://doi.org/10.1016/S0034-4257(02)00010-X

Sims, D. A., & Gamon, J. A. (2003). Estimation of vegetation water content and photosynthetic tissue area from spectral reflectance: a comparison of indices based on liquid water and chlorophyll absorption features. *Remote Sensing of Environment, 84*(4), 526-537. https://doi.org/10.1016/S0034-4257(02)00151-7

Stuart, M. B., McGonigle, A. J. S., & Willmott, J. R. (2019). Hyperspectral imaging in environmental monitoring: A review of recent developments and technological advances in compact field deployable systems. *Sensors, 19*(14), Article 3071. https://doi.org/10.3390/s19143071

Sun, G., Ding, Y., Wang, X., Lu, W., Sun, Y., & Yu, H. (2019). Nondestructive determination of nitrogen, phosphorus and potassium contents in greenhouse tomato plants based on multispectral three-dimensional imaging. *Sensors, 19*(23), Article 5295. https://doi.org/10.3390/s19235295

Sun, H., Liu, N., Wu, L., Chen, L., Yang, L., Li, M., & Zhang, Q. (2018). Water content detection of potato leaves based on hyperspectral image. *IFAC-PapersOnLine, 51*(17), 443-448. https://doi.org/10.1016/j.ifacol.2018.08.179

Sun, J., Yang, W., Zhang, M., Feng, M., Xiao, L., & Ding, G. (2021). Estimation of water content in corn leaves using hyperspectral data based on fractional order Savitzky-Golay derivation coupled with wavelength selection. *Computers and Electronics in Agriculture, 182*, Article 105989. https://doi.org/10.1016/j.compag.2021.105989

Tian, Y., & Zhang, L. (2012). Study on the methods of detecting cucumber downy mildew using hyperspectral imaging technology. *Physics Procedia, 33*, 743-750. https://doi.org/10.1016/j.phpro.2012.05.130

Vigneau, N., Ecarnot, M., Rabatel, G., & Roumet, P. (2011). Potential of field hyperspectral imaging as a non destructive method to assess leaf nitrogen content in Wheat. *Field Crops Research, 122*(1), 25-31. https://doi.org/10.1016/j.fcr.2011.02.003

Villegas, G., Liao, W., Criollo, R., Philips, W., & Ochoa, D. (2017). Detection of leaf structures in close-range hyperspectral images using morphological fusion. *Geo-Spatial Information Science, 20*(4), 325-332. https://doi.org/10.1080/10095020.2017.1399673

Wang, H., Chen, J., Lin, H., & Yuan, D. (2010). Research on effectiveness of hyperspectral data on identifying rice of different genotypes. *Remote Sensing Letters, 1*(4), 223-229. https://doi.org/10.1080/01431161.2010.481680

Wang, X., Zhang, Y., Ma, X., Xu, T., & Arce, G. R. (2018). Compressive spectral imaging system based on liquid crystal tunable filter. *Optics Express, 26*(19), Article 25226. https://doi.org/10.1364/oe.26.025226

Wang, Z., Hu, M., & Zhai, G. (2018). Application of deep learning architectures for accurate and rapid detection of internal mechanical damage of blueberry using hyperspectral transmittance data. *Sensors, 18*(4), Article 1126. https://doi.org/10.3390/s18041126

Williams, D., Britten, A., McCallum, S., Jones, H., Aitkenhead, M., Karley, A., Loades, K., Prashar, A., & Graham, J. (2017). A method for automatic segmentation and splitting of hyperspectral images of raspberry plants collected in field conditions. *Plant Methods, 13*(1), 1-12. https://doi.org/10.1186/s13007-017-0226-y

Yan, T., Xu, W., Lin, J., Duan, L., Gao, P., Zhang, C., & Lv, X. (2021). Combining multi-dimensional Convolutional Neural Network (CNN) with visualization method for detection of aphis gossypii glover infection in cotton leaves using hyperspectral imaging. *Frontiers in Plant Science, 12*, Article 604510. https://doi.org/10.3389/fpls.2021.604510

Yang, W., Yang, C., Hao, Z., Xie, C., & Li, M. (2019). Diagnosis of plant cold damage based on hyperspectral imaging and convolutional neural network. *IEEE Access, 7*, 118239-118248. https://doi.org/10.1109/ACCESS.2019.2936892

Yuan, L., Huang, Y., Loraamm, R. W., Nie, C., Wang, J., & Zhang, J. (2014). Spectral analysis of winter wheat leaves for detection and differentiation of diseases and insects. *Field Crops Research, 156*, 199-207. https://doi.org/10.1016/j.fcr.2013.11.012

Zhang, F., & Zhou, G. (2019). Estimation of vegetation water content using hyperspectral vegetation indices: A comparison of crop water indicators in response to water stress treatments for summer maize. *BMC Ecology, 19*(1), 1-12. https://doi.org/10.1186/s12898-019-0233-0

Zhang, J. C., Pu, R. L., Wang, J. H., Huang, W. J., Yuan, L., & Luo, J. H. (2012). Detecting powdery mildew of winter wheat using leaf level hyperspectral measurements. *Computers and Electronics in Agriculture, 85*, 13-23. https://doi.org/10.1016/j.compag.2012.03.006

Zhao, C., Liu, B., Piao, S., Wang, X., Lobell, D. B., Huang, Y., Huang, M., Yao, Y., Bassu, S., Ciais, P., Durand, J. L., Elliott, J., Ewert, F., Janssens, I. A., Li, T., Lin, E., Liu, Q., Martre, P., Müller, C., … & Asseng, S. (2017). Temperature increase reduces global yields of major crops in four independent estimates. *Proceedings of the National Academy of Sciences of the United States of America, 114*(35), 9326-9331. https://doi.org/10.1073/pnas.1701762114

Zhao, J., Pan, F., Li, Z., Lan, Y., Lu, L., Yang, D., & Wen, Y. (2021). Detection of cotton waterlogging stress based on hyperspectral images and convolutional neural network. *International Journal of Agricultural and Biological Engineering, 14*(2), 167-174. https://doi.org/10.25165/J.IJABE.20211402.6023